

# Quantitative Analysis of Plasmonic Metal Oxide Nanocrystal Ensembles Reveals the Influence of Dopant Selection on Intrinsic Optoelectronic Properties

Bharat Tandon<sup>†</sup>, Stephen L. Gibbs<sup>†</sup>, Benjamin Z. Zydlewski, Delia J. Milliron\*

*McKetta Department of Chemical Engineering, University of Texas at Austin,  
Austin, Texas 78712-1589, United States*

## Abstract:

Localized surface plasmon resonance (LSPR) arising from free charge carriers in doped metal oxide nanocrystals (NCs) has attracted abundant attention in the past decade for its potential in applications such as electrochromics, sensing, and photothermal therapy. While a lot is already known about LSPR of doped metal oxide NCs, there is still much to learn about the effect of dopant identity on the electronic structure of the host and, in particular, the effect on surface depletion layers. Here, using indium oxide as the host lattice, we discuss the contribution of a dopant to the electronic structure and rationalize an empirical understanding on how a particular dopant can impact surface depletion, carrier concentration, and carrier damping in doped metal oxide NCs. To do this, we leverage a slow injection synthesis to incorporate four different dopants (Sn, Zr, Ti, and Ce) in indium oxide NCs. For each dopant, we synthesized NCs with different radius but similar nominal doping level (~1 at%) and measured the optical response of dilute dispersions. This allowed us to deconvolute the effects of size and doping identity on LSPR. By fitting their plasmonic response to the heterogeneous ensemble Drude approximation, we extracted intrinsic electronic properties of the NCs such as surface depletion layer thickness, carrier concentration, and carrier damping, and rationalized the influence of dopant selection on each parameter. We find that the identity of the dopant does not have a significant impact on the extent of the depletion layer, but it does impact carrier concentration and damping. In general, dopants with a greater electropositivity, similar radius to the host atom, and a stable aliovalent oxidation state will have higher dopant activation, lower damping, and higher optical extinction. This study employs a broad sample set to empirically illustrate the effect of dopant identity on LSPR of doped metal oxide NCs and this new understanding will facilitate their implementation in different applications.

**Keywords:** LSPR, surface depletion, extinction coefficient, metal oxide, doping, nanocrystals

## Introduction:

The discovery of localized surface plasmon resonance (LSPR) in semiconductor nanocrystals (NCs) and in particular, doped metal oxide (MO) NCs has led to a significant surge in the attention being directed towards them.<sup>1-4</sup> This is mostly because, in recent times, LSPR has found applications in a wide variety of fields including photovoltaics,<sup>5</sup> photothermal therapy,<sup>6</sup> electrochromics,<sup>7-9</sup> sensing<sup>10</sup> and surface enhanced infrared spectroscopy.<sup>1</sup> The origin of this LSPR can be attributed to the presence of excess free charge carriers in the NCs which oscillate at resonant frequencies with the incident radiation. However, the maximum carrier concentration achievable for doped MO NCs is usually an order of magnitude smaller than that for conventional noble metal NCs.<sup>4</sup> Consequently, the LSPR maximum of doped MO NCs falls in the near- to mid-infrared region unlike noble metal NCs that exhibit LSPR in the visible range. Nonetheless, while the charge carriers in noble metal NCs are intrinsic, coming from the metal ions themselves, in

doped MO NCs, these charge carriers are a consequence of doping. Since the carrier concentration is dependent upon the extent of doping in NCs, doped MO NCs offer an added advantage of a compositionally tunable LSPR. We note here that this doping in NCs can be both intrinsic (self-doping) and/or extrinsic (aliovalent doping) in nature and the total carrier concentration may be a result of contributions from both types of doping.<sup>4</sup>

The LSPR of doped MO NCs is also influenced by the presence of charged impurities (dopants) in the host lattice which modifies the electronic structure, surface chemistry, generation of charge carriers, and carrier scattering mechanisms.<sup>4</sup> In general, there have been two governing criteria to predict how dopant selection impacts these properties: ionic radius and donor energy level with respect to the conduction band minimum (CBM). These factors are expected to determine the efficiency of free electron generation or dopant activation, and the nature and magnitude of electron scattering by dopant effects.<sup>11, 12</sup> More recently, additional factors impacting the plasmonic optical response have come to light, namely dopant heterogeneity within an ensemble of NCs and surface depletion.<sup>13-17</sup> In an ensemble of NCs there will inevitably be variation in the number of dopants incorporated into each NC. This results in a heterogeneous ensemble that artificially broadens the ensemble LSPR peak beyond the single particle intrinsic damping associated with plasmon dephasing. So, hypothetically, if a particular dopant tended to produce an ensemble with less dopant heterogeneity, one could use dopant selection as a strategy to minimize broadening of an ensemble response.

Furthermore, there has been a recent study on how size and doping level affect the depletion layer in Sn-doped  $\text{In}_2\text{O}_3$  ( $\text{Sn}:\text{In}_2\text{O}_3$ ) NCs.<sup>14, 18</sup> Surface states, which can be associated with adventitious water species such as hydroxyls, withdraw electrons from the bulk of the NC to establish an insulating shell (the surface depletion layer) of low carrier concentration near the surface.<sup>16</sup> Ionized dopants screen the surface charge, with their concentration theoretically determining the depletion width. Although in this simple model depletion effects are expected to be independent of dopant composition beyond their formal charge, there has not been a systematic study for other dopants other than tin. Therefore, while a lot of understanding has been developed for  $\text{Sn}:\text{In}_2\text{O}_3$  NCs, key questions remain regarding the role of a dopant selection in governing LSPR. Do certain dopants incorporate into the indium oxide host lattice more homogeneously than others? How do dopant selection and dopant activation influence the surface depletion width in doped MO NCs? Is the depletion model, as developed using  $\text{Sn}:\text{In}_2\text{O}_3$  NCs, universally applicable irrespective of the dopant? How will this depletion layer at the surface impact the ability of different doped MO NCs to absorb the incident radiation i.e., the extinction coefficient?

Addressing these questions has been challenging since there has previously not been a library of doped NCs with a variety of incorporated aliovalent dopants whose other characteristics were consistent, based on a common synthetic mechanism. Fortunately, over the last few years, synthetic methods have advanced such that a diverse pool of dopants might be compatible with a single host.<sup>11, 12, 19</sup> More specifically, multiple different dopants can now be incorporated in the  $\text{In}_2\text{O}_3$  lattice (a widely explored and commercially relevant MO system) thus empowering us to investigate now the effect of dopant composition on the electronic structure, surface depletion, and, consequently, the optical properties of doped MO NCs. At the same time, the development of slow-injection synthesis in the past few years has allowed the synthesis of doped MO NCs in high-yield with regular shapes and tunable sizes.<sup>20, 21</sup>

Thus, using a slow-injection synthesis, we here prepare 1% doped  $\text{In}_2\text{O}_3$  NCs of different sizes with either Sn, Ce, Ti, or Zr as the dopant. The dopants were chosen to have different energy levels with respect to the CBM of the  $\text{In}_2\text{O}_3$  to gauge the effect of energy level alignment on the LSPR. An estimate of the dopant energy level with respect to the  $\text{In}_2\text{O}_3$  CBM can be made by comparing their electronegativity values with In since the CBM is derived largely from In 5s orbitals (Table 1).<sup>11</sup> Even though all the dopants carry the same aliovalent charge of +1, which suggests that their electrostatic scattering of charge carriers would be similar, they possess varying ionic radii (Table 1), which should have an impact on the rate of electron scattering and thus the LSPR linewidth due to differences in induced lattice strain.

**Table 1:** Ionic radii and electronegativity for dopant and host ions employed in this work and the difference in ionic radius ( $\Delta\text{IR}_{\text{In}}$ ) and electronegativity ( $\Delta\text{EN}_{\text{In}}$ ) between the dopant and the host atoms (In). Ionic radii acquired from reference 22.

<b>Metal (Valence)</b>	<b>Ionic Radius (pm)</b>	<b><math>\Delta\text{IR}_{\text{In}}</math> (pm)</b>	<b>Electronegativity</b>	<b><math>\Delta\text{EN}_{\text{In}}</math></b>
<b>Ti (4+)</b>	74.5	-19.5	1.54	-0.24
<b>Sn (4+)</b>	83	-11	1.96	+0.18
<b>Zr (4+)</b>	86	-8	1.33	-0.45
<b>In (3+)</b>	94	-	1.78	-
<b>Ce (4+)</b>	101	+7	1.12	-0.66

Importantly, leveraging independent size and doping control, we aimed not only to assess these differences among dopants, but also to test the effect of NC size, all for a common host lattice of  $\text{In}_2\text{O}_3$ . The long wavelength of the LSPR peak and small NC size means that the electric field of incoming light is approximately constant across the NC, placing these NCs in the quasistatic regime. Yet, recent work has shown that the LSPR in Sn: $\text{In}_2\text{O}_3$  NCs has a strong size-dependence due to surface effects such as depletion and surface damping.<sup>14, 23</sup> The relative contribution of surface effects to the overall optical response must be discerned in order to probe dopant composition effects. For example, if surface damping dominates bulk damping (when the radius is smaller than the bulk mean free path),<sup>17</sup> LSPR characteristics will be less sensitive to differences in bulk damping between dopants.

After synthesizing doped  $\text{In}_2\text{O}_3$  NCs of different radius and dopant composition, we measured the optical response of their dispersions, all of which lie in the near- to mid-infrared range. Their plasmonic responses were then fitted with a heterogeneous ensemble Drude approximation (HEDA) model which accounts for heterogeneity in doping and size, and surface depletion effects.<sup>17</sup> This fitting was then used to extract intrinsic properties of the NCs such as carrier concentration, depletion width, and damping constant. We noticed that for all dopants, with an increase in the radius of the NCs, there was an increase in the carrier concentration (i.e., dopant activation), decrease in the depleted volume fraction, and a decrease in the damping constant, which is in good agreement with the prediction of the surface depletion model and is consistent with earlier reported trends for Sn: $\text{In}_2\text{O}_3$  NCs. This validates that the depletion model developed

using Sn:In<sub>2</sub>O<sub>3</sub> NCs is an accurate representation of intra-NC charge distribution for a wide range of dopants.

**Table 2:** Summary of the STEM radius and ICP-AES doping percentages of different doped In<sub>2</sub>O<sub>3</sub> NCs synthesized through the slow-injection procedure.

Sample Description	ICP-AES doping %	XPS doping %	STEM Radius
Sn:In <sub>2</sub> O <sub>3</sub>	0.88 ± 0.06	0.88	4.2 ± 0.3 nm
	0.9 ± 0.05	0.89	4.9 ± 0.3 nm
	0.89 ± 0.04	0.96	6.1 ± 0.4 nm
	0.88 ± 0.04	1.03	7.7 ± 0.4 nm
	0.87 ± 0.02	0.95	8.9 ± 0.4 nm
Ti:In <sub>2</sub> O <sub>3</sub>	0.87 ± 0.01	0	5.2 ± 0.2 nm
	1.17 ± 0.02	0	5.5 ± 0.3 nm
	1.09 ± 0.03	0	7.0 ± 0.2 nm
	1.13 ± 0.02	0	12.5 ± 1.2 nm
Ce:In <sub>2</sub> O <sub>3</sub>	1.13 ± 0.09	0.87	5.3 ± 0.3 nm
	0.69 ± 0.21	0.79	5.7 ± 0.7 nm
	1.24 ± 0.1	1.13	6.9 ± 0.8 nm
	1.01 ± 0.08	0.73	7.7 ± 1.0 nm
	0.88 ± 0.09	0.95	9.1 ± 1.1 nm
Zr:In <sub>2</sub> O <sub>3</sub>	1.03 ± 0.03	2.53	3.1 ± 0.3 nm
	0.91 ± 0.03	1.21	4.1 ± 0.2 nm
	0.87 ± 0.01	1.62	5.0 ± 0.4 nm
	1.53 ± 0.1	2.62	7.1 ± 0.7 nm
	1.07 ± 0.1	1.87	8.3 ± 0.8 nm

Our results showed that the effects of surface depletion are prominent among all studied dopants and that the extent of the surface depletion layers into the NC was not significantly different among NCs of the same size and different dopants. As well, the ensemble heterogeneity in doping was nearly indistinguishable among NCs of the same size. However, there was significant variation in the LSPR peak width and energy, implying that these dopants are far from equivalent. From the parameters extracted by HEDA, we found that more electropositive dopants having a single stable oxidation state have higher dopant activation and thus higher carrier concentration. Also, dopants of greater electropositivity and lesser  $\Delta I_{R_{In}}$  minimized carrier damping. Taken together, these

results outline the necessary traits for high extinction and narrow linewidth LSPR from doped MO NCs.

## Result and Discussion

### 1. Synthesis and characterization of doped $\text{In}_2\text{O}_3$

To determine the influence of dopant on the surface depletion effects and extinction coefficients in doped  $\text{In}_2\text{O}_3$  NCs, we first synthesized doped  $\text{In}_2\text{O}_3$  NCs with different radius and dopants through the slow-injection synthesis developed by the Hutchinson group<sup>21</sup> (Figure S1). Specific details regarding the nanocrystal synthesis and characterization can be found in Text S1 of supporting information. Table 2 provides a summary of all the samples synthesized and a nominal doping percentage of 1% for all dopants obtained from inductively-coupled plasma atomic emission spectroscopy (ICP-AES).

The doping percentage was kept at  $\sim 1\%$  for several reasons. (1) It is achievable for all dopants selected in the  $\text{In}_2\text{O}_3$  lattice. (2) The volume fraction of the depletion layer is significant for small doping percentages, so our experiments will be sensitive to variations in the depletion width with change of the dopant. (3) At high doping percentages, dopants may undergo clustering<sup>24</sup> which can complicate the physical interpretation of the optical data. On the other hand, at smaller doping concentrations, the dopants have a dilute distribution in the NC and are less likely cluster.<sup>25</sup>

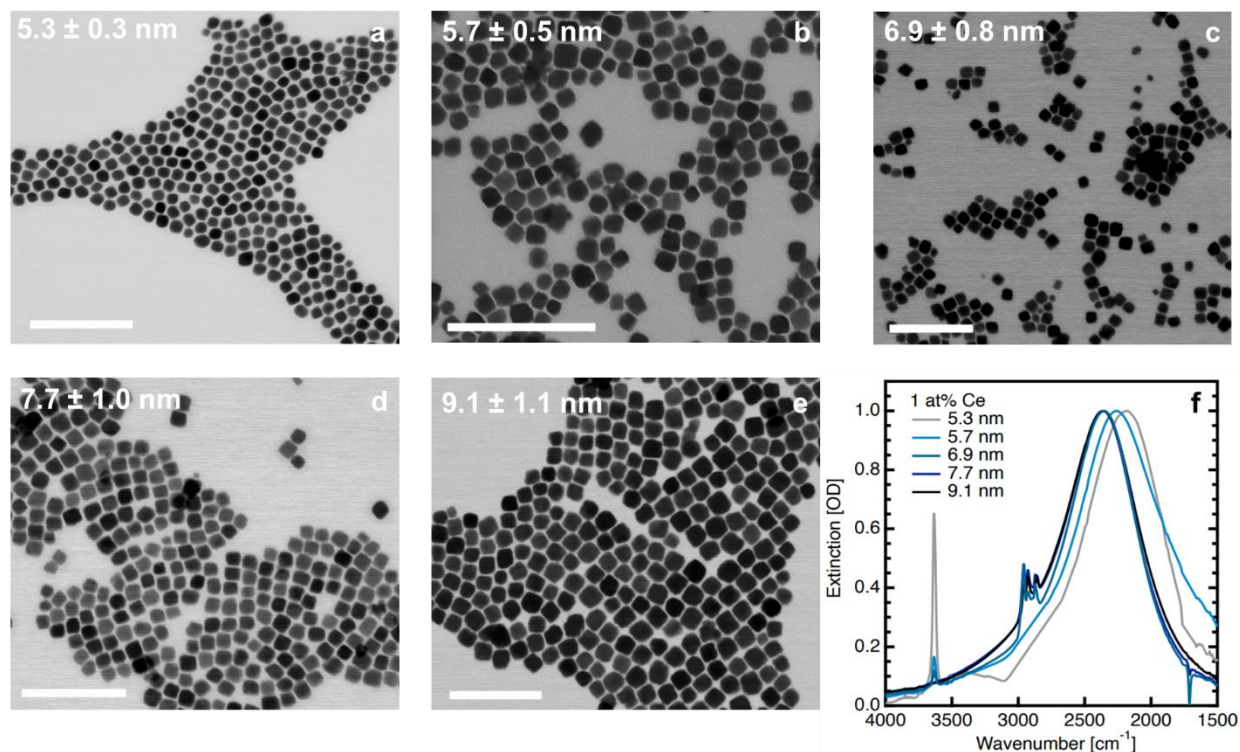


**Figure 1:** (a-e) STEM images. All scale bars are 100 nm, and (f) normalized extinction spectra, for 1% Ce: $\text{In}_2\text{O}_3$  NCs of increasing radius.

To qualitatively assess the radial distribution of dopants, we compare the near-surface doping percentage obtained from X-ray photoelectron spectroscopy (XPS) technique with the overall dopant concentration determined by digesting the NCs, analyzed by ICP-AES. Interestingly, we

find that while Ce and Sn are uniformly doped throughout the NC volume, Zr is segregated preferentially toward the surface and Ti is segregated toward the core (no Ti is observable by XPS). This is an important observation as the radial distribution of dopant has been found to influence the dopant activation (number of carriers donated by each dopant), carrier scattering, and surface depletion width.<sup>26, 27</sup>

Scanning transmission electron microscopy (STEM) images acquired for different sizes of 1% Ce:In<sub>2</sub>O<sub>3</sub> NCs (5.3-9.1 nm radius) show uniform size distribution (Figure 1a-e). STEM images for other doped In<sub>2</sub>O<sub>3</sub> NCs along with their particle size distribution analysis are provided in the supporting information (Figure S2-S4), along with normalized extinction spectra (Figure S5).

## 2. Trends in Ensemble LSPR Peaks

Even before fitting spectra to a model to extract intrinsic optoelectronic properties, we can draw some conclusions about the NC ensemble by analyzing peak position, lineshape, and intensity. We notice that for Sn:In<sub>2</sub>O<sub>3</sub> and Ti:In<sub>2</sub>O<sub>3</sub> NCs, the LSPR energy increases with an increase in the NC radius (Figure 2a) which is consistent with previous observations in Sn:In<sub>2</sub>O<sub>3</sub> NCs of increasing carrier concentration corresponding to an increase in the fraction of activated dopants

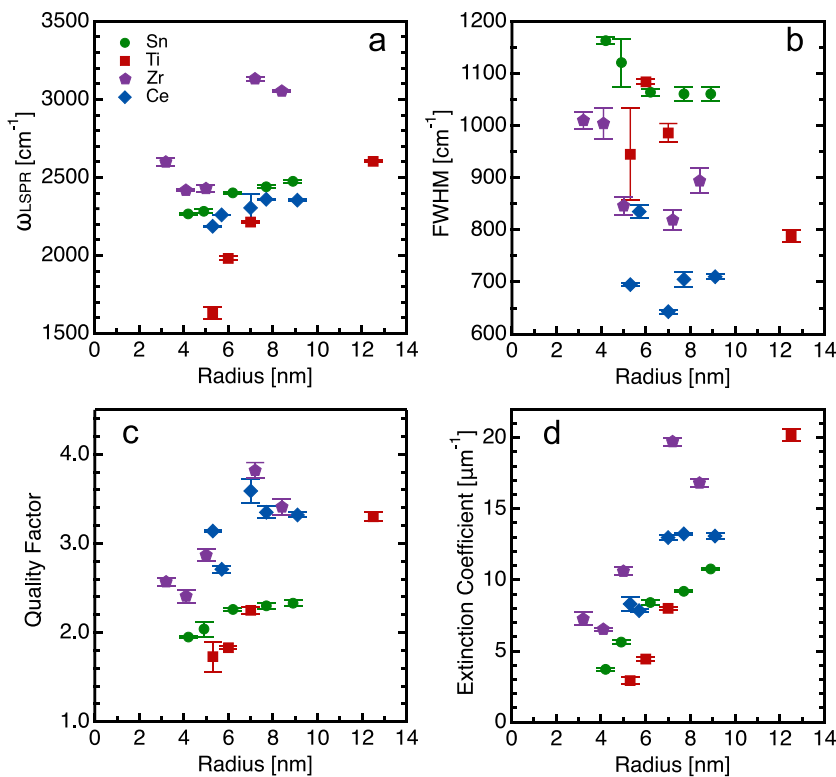


**Figure 2:** Trends in (a) LSPR energy, (b) FWHM, (c) volume-normalized extinction coefficient, and (d) quality factor with nanocrystal radius for different doped In<sub>2</sub>O<sub>3</sub> NCs. Error bars represent standard deviation of measured properties acquired from at least three optical spectra collected at differing dilutions.

(dopant activation) with size.<sup>14</sup> Even for Zr:In<sub>2</sub>O<sub>3</sub>, a similar trend is observed except some samples exhibit higher than expected LSPR energy. This is likely due to an unintended variation in the

doping percentage between samples, which was most significant in Zr doping (Table 2). For, Ce:In<sub>2</sub>O<sub>3</sub> NCs also, with an increase in NC radius, the LSPR peak energy was found to increase although it saturated for sizes above 7 nm in radius. In the following section, after fitting spectra to the HEDA model, we discuss the probable reasons for this common trend, which was consistently observed for different dopants.

While all the dopants show the same qualitative behavior on the increase of the NC radius, the LSPR energy for a given size NC does depend on dopant selection. We note that while there is minimal variation in doping level across all samples, except some significant variation in the over-doped Zr 7.1 nm sample (1.53 at%), most fall close enough to 1 at% overall to draw meaningful comparisons between different dopants. As shown in Figure 2a, the peak position ( $\omega_{\text{LSPR}}$ ) for all samples increases with size and, in general, at a given NC radius the peak position, from high to low, trends as Zr>Sn>Ce>Ti. This indicates that all dopants are not equivalent in the In<sub>2</sub>O<sub>3</sub> lattice and some are more efficient than others at contributing charge carriers to sustain LSPR at higher  $\omega_{\text{LSPR}}$  due to a higher free carrier concentration.

Likewise, there is a clear, consistent spread among FWHM (full width at half maxima), quality factor, and extinction coefficient values for the differing dopants, further emphasizing that there is a significant difference in how each dopant alters the host lattice and the NC optical response. Quality factor, a ratio of the LSPR peak energy to its FWHM, is a common figure of merit for comparing the optical response of plasmonic particles. Our measurements indicate that among these samples, Ce and Zr obtain the highest quality factors (Figure 2c) but for differing reasons. While Zr doping has highest LSPR peak energies (Figure 2a), Ce doping results in the narrowest FWHM (Figure 2b). On the other hand, even though Sn doping shows consistently higher FWHM than Ti doping, the higher energy LSPR peaks resulting from Sn doping drive their quality factors above those for Ti doping. Because quality factor is an indirect measure of near-field enhancement potential, a higher quality factor is more desirable for applications involving coupling between plasmons and their environment, and should lead to higher peak absorption of the incident radiation. Considering differences in quality factor and free electron concentration, we expect that for the same doping level and NC size, Zr:In<sub>2</sub>O<sub>3</sub> NCs should possess the highest values of the peak extinction coefficients and Ti:In<sub>2</sub>O<sub>3</sub> NCs the lowest.

We observed that the volume normalized extinction coefficient increases with size (Figure 2d), consistent with prior work on Sn:In<sub>2</sub>O<sub>3</sub> NCs, which attributed this increase to an increase in dopant activation.<sup>14, 17</sup> When comparing NCs of similar size, we found that the extinction coefficients generally trended as Zr>Ce>Sn>Ti (see Figure S6-S9 for extinction measurements). Therefore, extinction coefficient values follow the same trend as LSPR quality factor, at both small and large NC radius. The absolute values of the extinction coefficients are in the same range as previously reported values for undoped and Sn:In<sub>2</sub>O<sub>3</sub> NCs of different doping percentages and radius.<sup>14</sup> Interestingly, the extinction of all 1 at% doped samples increases with size and does not reach a saturation point as was the case for 5 at% Sn above ~6 nm in radius.<sup>14</sup> Knowing that the effects of surface depletion layers are more prominent for lower doped NCs, one would reasonably expect that the size effects of surface depletion layers would persist to larger volumes for lesser doped samples, such as these 1 at% samples. However, there are many factors that influence these trends in extinction coefficients, peak position, FWHM, and quality factors, and heterogeneous

broadening can misguide such qualitative interpretations, which warranted a more quantitative assessment.

### 3. Extracting intrinsic optical and electronic properties from ensemble measurements

For a particular doping percentage these measurables result from contributions from the charge carrier concentration, dopant activation, damping of charge carriers, and surface depletion effects. Further, when measuring NC ensembles, polydispersity in size and doping percentage also influences the observed LSPR. To elucidate the contribution of each of the aforementioned parameters in determining the non-equivalency of dopants in  $\text{In}_2\text{O}_3$  NCs, we fitted the optical response of our NCs with the recently developed heterogeneous ensemble Drude approximation (HEDA) model which accounts for ensemble heterogeneity in size and doping, while also extracting intrinsic electronic properties. To run this fit procedure, the average and standard deviation in NC radius must be known, typically acquired through STEM or small angle X-ray scattering, as well as the concentration of NCs in the dispersion, typically acquired through ICP-AES. With these inputs, along with a few other material constants, the HEDA model then fits for the average charge carrier concentration, the standard deviation in charge carrier concentration among NCs in the ensemble, the bulk mean free path that reflects the influence of carrier damping, and the surface depletion layer thickness.<sup>17</sup> The HEDA model was earlier validated using  $\text{Sn}:\text{In}_2\text{O}_3$  NCs and this is the first time applying it to other compositions, though the implementation is straightforward, especially because  $\text{In}_2\text{O}_3$  is the common host lattice. With these results in hand, we can characterize the intrinsic electronic properties of the average NC in an ensemble distinguished from the convoluting effects of ensemble heterogeneity. A more detailed procedure for HEDA modeling can be found in Text S3.

A representative set of extinction spectra for dilutions of  $\text{Ce}:\text{In}_2\text{O}_3$  NCs illustrate the high-quality fits obtained with the HEDA model (Figure 3a). Fits with similar quality were obtained for all NCs, irrespective of size or dopant (Figure S10-S13). As expected, the trend in LSPR peak energy matches that of the charge carrier concentration,  $n_e$ , (Figure 3b) which decreases in the order  $\text{Zr} > \text{Sn} > \text{Ce} > \text{Ti}$ . The carrier concentration for Sn and Ce is nearly constant with an increase in the NC radius. In contrast, for Zr and Ti there is a more noticeable increase with size. To uncover the reasons for these trends we must consider the fraction of activated dopants (dopant activation) of each sample. Dopant activation is calculated as the ratio of free charge carriers to dopants in the average NC in the ensemble:

$$\text{Dopant Activation} = \frac{f_e n_e}{N_D} \quad (1)$$

Where  $f_e$  is the volume fraction of the NC that remains undepleted, or what we term as the *electron accessible volume fraction*, and  $N_D$  is the concentration of dopant atoms as determined by ICP-AES.

For all dopants, with an increase in the NC radius, the dopant activation gradually increases, signifying that a greater fraction of the overall dopants contributes towards the generation of charge carriers (Figure 3c). Dopants can be inactivated through four typical mechanisms. (i) The clustering of dopant ions can form low energy trap states preventing generation of charge

carriers.<sup>24</sup> (ii) The existence of the surface depletion layer causes dopants present in the depletion layer to not contribute any significant carrier density to the plasmonic core.<sup>16</sup> (iii) The nonuniform radial distribution of dopants causes dopants situated close the surface to be more likely to be deactivated through compensating defects like oxygen interstitials than those in the core of the NC.<sup>26</sup> (iv) The change in the oxidation state of the dopant, for example a conversion of  $\text{Ce}^{4+}$  to  $\text{Ce}^{3+}$  or  $\text{Ti}^{4+}$  to  $\text{Ti}^{3+}$ , resulting from localization of free electrons, can decrease the electron concentration relative to dopant content.<sup>11</sup>

As mentioned before, we do not expect that at dopant concentrations of  $\sim 1$  at % dopant clustering effects will be significant. Moreover, since the dopant density is independent of the size of the NC, the increasing dopant activation with radius is not likely due to a reduced clustering of dopant ions. Thus, we turn to surface depletion, dopant distribution, and oxidation states to explain our trends. Indeed, we see that, as shown in Figure 3d, the electron accessible volume fraction,  $f_e$ , increases with size for all dopants.

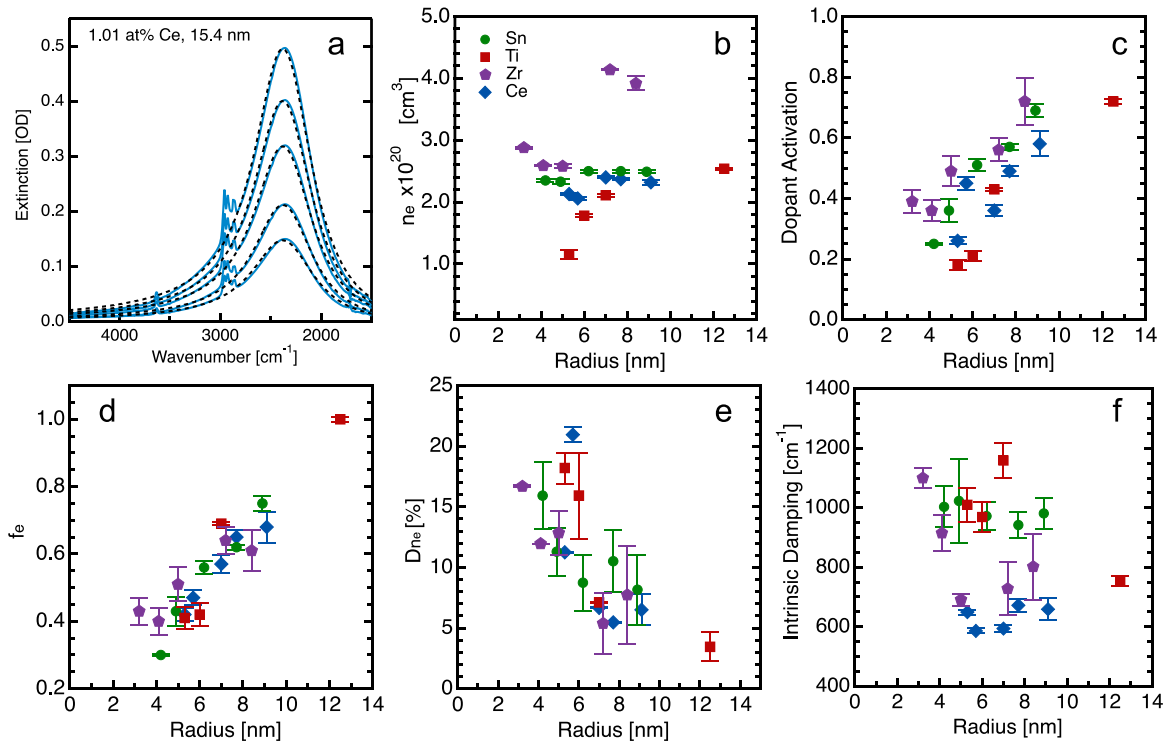


**Figure 3:** (a) Representative HEDA model fits to LSPR spectra of dispersions of Ce:In<sub>2</sub>O<sub>3</sub> NC ensembles for 5 different dilution factors. Variation in (b) carrier concentration, (c) dopant activation, (d) electron accessible volume fraction, (e) carrier concentration polydispersity, and (f) intrinsic electron damping, with increase in radius of NC for different doped In<sub>2</sub>O<sub>3</sub> NCs. Error bars represent standard deviation of fit results acquired from fitting at least three optical spectra of differing dilution factors.

This increase in  $f_e$  increases the fraction of dopants that are in the plasmonic core and able to contribute to carrier generation (Figure 3c), ultimately driving up the volume-normalized extinction coefficient (Figure 2d). Of note, for the same size, the  $f_e$  values don't vary significantly

between different dopants and this trend is quantitatively consistent among all sizes within the error of our fits. This is understandable since previous reports have suggested that the surface states driving formation of the depletion region are associated with surface hydroxyls that should be similarly present regardless of the dopants.<sup>13,28</sup> With doping as dilute as 1%, nearly all the surface hydroxyl groups are expected to be on indium sites and the band bending is dependent only on dopant charge, not composition. This shows that dopant selection does not have a large impact on the extent of the surface depletion layer and reinforces the universal impact of surface depletion layers in a variety of doped  $\text{In}_2\text{O}_3$  NCs.

We must now consider how surface depletion might have a different impact on samples of differing dopant spatial distribution. Both samples which are uniformly doped,  $\text{Sn}:\text{In}_2\text{O}_3$  and  $\text{Ce}:\text{In}_2\text{O}_3$  NCs, show minimal change in  $n_e$  with size, but an increase in dopant activation. These two trends are consistent when you consider the effect of the depletion layer. As the depletion layer occupies less and less of the overall volume fraction of the NC, the fraction of activated dopants will increase, but  $n_e$  in the plasmonic core will remain the same. However, for  $\text{Zr}:\text{In}_2\text{O}_3$  and  $\text{Ti}:\text{In}_2\text{O}_3$  NCs the dopants are surface-segregated and core-segregated, respectively. Because dopants closer to the surface are more likely to be deactivated, we would expect overall dopant activation for  $\text{Zr}:\text{In}_2\text{O}_3$  to be lower than that for  $\text{Sn}:\text{In}_2\text{O}_3$  and  $\text{Ce}:\text{In}_2\text{O}_3$ . For the same reason, we would expect dopant activation for  $\text{Ti}:\text{In}_2\text{O}_3$  to be higher than that for  $\text{Sn}:\text{In}_2\text{O}_3$  and  $\text{Ce}:\text{In}_2\text{O}_3$ . We find the reverse to be true (Figure 3c). Even while segregated to the surface, Zr dopants have the highest dopant activation of all, indicating that electropositivity, and therefore donor level alignment, is more crucial to dopant activation than proximity to the surface. And even while segregated to the core, Ti dopants have the lowest dopant activation of all. This would indicate that the ability for Ti to stabilize in more than one oxidation state ( $\text{Ti}^{4+}$  and  $\text{Ti}^{3+}$ ), along with its relatively low electropositivity are more influential in determining dopant activation than proximity to the surface.

The polydispersity in carrier concentration among NCs in the ensemble also shows no dependence on dopant choice within the error of our fitting (Figure 3e). This rules out any contribution of peak narrowing or broadening because one particular dopant is distributed more or less uniformly across a NC ensemble. This consistency suggests that the heterogeneity observed herein, which is consistently higher than the theoretical minimum based on Poissonian statistics, may be the best achievable with the slow-growth synthesis method used for all the analyzed samples. As a result, the trends in intrinsic damping directly mirror those of the ensemble FWHM (Figure 3f).

For a given NC radius, different dopants have significantly different values of dopant activation. This means that it might be more feasible for some dopants to donate charge carriers than others. Zr has the highest dopant activation despite surface-segregation, which was shown to reduce activation of Sn dopants,<sup>26,27,29</sup> and Ti is the least activated dopant in  $\text{In}_2\text{O}_3$  lattice in spite of core-segregated doping, which should enhance Sn dopant activation. The trend in dopant activation is clearly reflected in Figure 3c where for a similar doping concentration and NC radius, Zr doping in  $\text{In}_2\text{O}_3$  produces the highest carrier concentration and Ti doping produces the lowest carrier concentration.

In sum, our results reveal how the relevant dopant selection criteria of donor energy level and ionic radius impact the resulting LSPR properties. In general, an increase in the dopant activation with

increase in NC radius is driven by an increase in the electron accessible volume fraction, which we've learned is rather independent of the choice of dopant. However, we do observe measurable differences in the dopant activation for different dopants at the same NC size. We attribute this to two probable contributing factors. First, it could be attributed to their energy level with respect to the  $\text{In}_2\text{O}_3$  CBM. Dopants which are situated close to the CBM (Ti and Sn) are expected to have considerably lower dopant activation as compared to those situated far above it (Zr and Ce). Second, is the stability of the dopant oxidation state. We note here that based purely on electronegativity, we expect Ce to have higher dopant activation than Zn and Sn at the same NC radius, but this is not the case since  $\text{Ce}^{4+}$  can readily convert to  $\text{Ce}^{3+}$ .<sup>11</sup> Similarly, even though Ti is expected to have higher dopant activation than Sn (more electropositive than Sn), Ti has lower than expected dopant activation, likely due to spontaneous conversion of  $\text{Ti}^{4+}$  to  $\text{Ti}^{3+}$ , similar to  $\text{Ce}^{4+}$ .

Comparing NCs of similar size, we expect any difference in scattering of charge carriers in doped  $\text{In}_2\text{O}_3$  NCs can be attributed to differences in ionized impurity scattering, which occurs due to charged defects in the lattice and their induced strain.<sup>14,30</sup> Since all the dopants have approximately the same nominal doping percentage and all ionized defects should have +1 charge, the density of charged defects in the lattice is not likely to be very different for different dopants. The carrier scattering, then, should be governed by the energy level of the dopant incorporated and the ionic radius. Previous reports suggest that dopants whose energy levels are situated far away from the  $\text{In}_2\text{O}_3$  CBM tend to participate less in ionized impurity scattering than situated close to it.<sup>11, 12</sup> Further, the ionic radius, if very different from the host metal atom, can cause significant lattice strain that also increases scattering. Based on this hypothesis, Ce and Zr are anticipated to scatter the carriers much less strongly than Ti and Sn, which is consistent with experimental LSPR linewidth (Figure 2b) and damping constants obtained through the HEDA fitting (Figure 3f). We note that it is important to consider both dopant energy level and ionic radius because, judging solely based off donor level would indicate that the damping of Ti would be less than that of Sn, which is not the case. We attribute the higher-than-expected damping of Ti to its exceedingly small ionic radius in comparison to  $\text{Sn}^{4+}$  and  $\text{In}^{3+}$  (Table 1).

We can go further in our understanding of how doping and size independently effect the LSPR peak characteristics by deconvoluting the damping that comes as a result of bulk damping vs that of surface damping. The total damping,  $\Gamma_{total}$ , of the average NC in an ensemble, as calculated from the Drude free electron model,<sup>17</sup> can be represented as the following.

$$\Gamma_{total} = \frac{(3\pi^2)^{\frac{1}{3}}\hbar}{m_e^*} n_e^{\frac{1}{3}} \left( \frac{1}{l_{MFP}} \right) \quad (2)$$

Where  $m_e^*$  and  $l_{MFP}$  are the effective mass and mean free path of a free electron, respectively. When the radius of the NC is similar to or smaller than the mean free path of an electron in the bulk,  $l_{bulk}$ , then the surface of the NC becomes prominent in determining the overall rate of electron scattering, effectively shortening the mean free path from its bulk value. To account for this, we can split the mean free path into bulk and surface scattering terms.

$$\Gamma_{total} = \frac{(3\pi^2)^{\frac{1}{3}}\hbar}{m_e^*} n_e^{\frac{1}{3}} \left( \frac{1}{l_{bulk}} + \frac{1}{\frac{4}{3}r_{NC}f_e^{\frac{1}{3}}} \right) = \Gamma_{bulk} + \Gamma_{surface} \quad (3)$$

where

$$\Gamma_{bulk} = \frac{(3\pi^2)^{\frac{1}{3}}\hbar}{m_e^*} n_e^{\frac{1}{3}} \left( \frac{1}{l_{bulk}} \right) \quad (4)$$

$$\Gamma_{surface} = \frac{(3\pi^2)^{\frac{1}{3}}\hbar}{m_e^*} n_e^{\frac{1}{3}} \left( \frac{1}{\frac{4}{3}r_{NC}f_e^{\frac{1}{3}}} \right) \quad (5)$$

Previously it was shown that for 5 at% Sn:In<sub>2</sub>O<sub>3</sub>, surface damping exceeds bulk damping at NC radii ~8 nm and smaller.<sup>14</sup> It is important to know this crossover point, because as you move to smaller sizes, and surface damping becomes heavily dominant, the LSPR peak properties of interest such as FWHM, extinction, and quality factor are more a function of the size of the NC than the bulk properties such as quantity or identity of dopants. For this reason, we found it imperative to tease out the crossover point of surface damping dominant and bulk damping dominate for our samples (Figure 4).

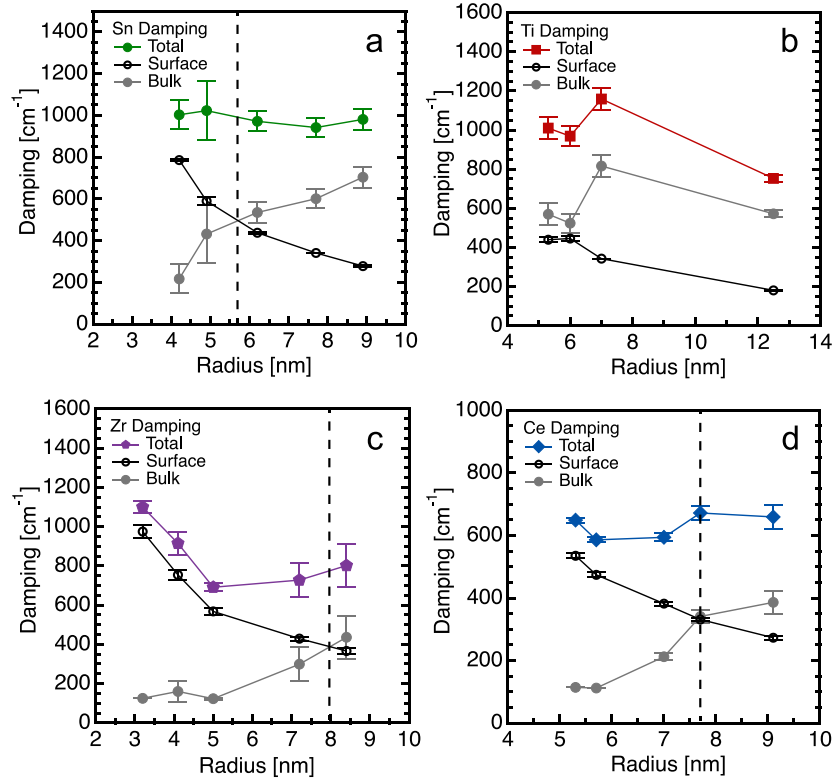


**Figure 4.** Total, surface, and bulk damping for 1 at% (a) Sn, (b) Ti, (c) Zr, and (d) Ce across a range of sizes. The vertical dashed line indicates the crossover radius below which surface damping becomes dominant over bulk damping. Error bars represent standard deviation of fit results acquired from fitting at least three optical spectra of differing dilution factors.

For a heavily damped material with a large bulk damping constant, we would expect surface damping to only become significant at very small sizes. Therefore, for dopants that magnify carrier damping, we expect that the crossover frequency occurs at smaller sizes than for dopants that mitigate carrier damping. This is exactly what we see. For Sn, the crossover radius is reached around 5.6 nm (Figure 4a), slightly smaller than for Zr or Ce (8 and 7.8 nm, respectively). This directly reflects the intrinsic damping values (Figure 3f).<sup>17</sup> We never reach a radius small enough for which the surface damping exceeds bulk damping for Ti (Figure 4b). This is consistent with Ti being the most heavily damped system. These crossover radii not only inform us about which dopants have less bulk damping contributions, they also inform of when we expect our system to be less size-dependent and more composition-dependent in its LSPR characteristics.

## Conclusion

In conclusion, using the slow-injection procedure, we synthesized a series of ~1% doped In<sub>2</sub>O<sub>3</sub> NCs with dopants having different energy levels with respect to the CBM of In<sub>2</sub>O<sub>3</sub>. We observe that even though all the dopants are aliovalent, they have non-equivalence in a lot of optical and electronic parameters. Extracting these parameters from their LSPR data through the HEDA model, it is revealed that while some dopants such as Zr are highly activated and do not scatter electrons considerably, dopants such as Ti have low dopant activation and cause significant damping of the free carrier oscillations. Consequently, Zr:In<sub>2</sub>O<sub>3</sub> leads to high carrier concentration, high LSPR energy and extinction coefficients whereas Ti:In<sub>2</sub>O<sub>3</sub> NCs generate low carrier concentration which is ultimately responsible for their low LSPR energy and extinction coefficients. Furthermore, even though there is appreciable difference in the optical response, for a particular NC radius, doped In<sub>2</sub>O<sub>3</sub> NCs have the same surface depletion width irrespective of the dopant. This makes surface depletion a characteristic property of the host NC with insignificant variations due to the dopant. Subsequently, all doped In<sub>2</sub>O<sub>3</sub> NCs follow the same qualitative trend of a decrease in the depletion width with an increase in the NC radius, regardless of the dopant employed, validating the universality of surface depletion model in doped indium oxide. Lastly, we explicitly deconvoluted the effects of surface and bulk damping for each dopant. By measuring the crossover radius, we have reported a metric to track the relative contributions of surface and bulk scattering, which is important when deciding how to modify doped metal oxide NCs to achieve desired plasmonic benchmarks such as extinction and quality factor. Our results suggest that it is essential to consider (i) the energy level of the incorporated dopant, (ii) the possible oxidation states (iii) and the ionic radius to predict the optical and electronic properties of a doped metal oxide NCs. Choosing a dopant with high electropositivity and stable aliovalent state can go a long way in ensuring a system that could ultimately turn commercially significant. Elucidating the role of dopant in determining the carrier concentration, carrier damping and surface depletion fills an important information gap and is likely to influence their implementation in all forthcoming investigations of both fundamental and applicative nature.

## Supporting Information

Details of nanocrystal synthesis and characterization (STEM, XRD, FTIR) and HEDA fitting to the LSPR spectra of doped In<sub>2</sub>O<sub>3</sub> NCs along with fits and parameters obtained are provided in the supporting information and can be accessed free of charge from the ACS Publications website.

## Author Information

†B. Tandon and S. L. Gibbs contributed equally to the manuscript.

\*E-mail: milliron@che.utexas.edu.

The authors declare no competing financial interest.

## Acknowledgements

This research was supported by the National Science Foundation (NSF), including CHE-1905263 and a Graduate Research Fellowship under Award Number (DGE-1610403, S.L.G.). Additional support came from the Welch Foundation (F-1848).

## References

1. Willets, K. A.; Duyne, R. P. V., Localized Surface Plasmon Resonance Spectroscopy and Sensing. *Ann. Rev. Phys. Chem.* **2007**, *58*, 267-297.
2. Faucheaux, J. A.; Stanton, A. L. D.; Jain, P. K., Plasmon Resonances of Semiconductor Nanocrystals: Physical Principles and New Opportunities. *J. Phys. Chem. Lett.* **2014**, *5*, 976-985.
3. Tandon, B.; Ashok, A.; Nag, A., Colloidal Transparent Conducting Oxide Nanocrystals: A New Infrared Plasmonic Material. *Pramana* **2015**, *84*, 1087-1098.
4. Agrawal, A.; Cho, S. H.; Zandi, O.; Ghosh, S.; Johns, R. W.; Milliron, D. J., Localized Surface Plasmon Resonance in Semiconductor Nanocrystals. *Chem. Rev.* **2018**, *118*, 3121-3207.
5. Atwater, H. A.; Polman, A., Plasmonics for Improved Photovoltaic Devices. *Nat. Mater.* **2010**, *9*, 205-213.
6. Jain, P. K.; Huang, X.; El-Sayed, I. H.; El-Sayed, M. A., Noble Metals on the Nanoscale: Optical and Photothermal Properties and Some Applications in Imaging, Sensing, Biology, and Medicine. *Acc. Chem. Res.* **2008**, *41*, 1578-1586.
7. Garcia, G.; Buonsanti, R.; Runnerstrom, E. L.; Mendelsberg, R. J.; Llordes, A.; Anders, A.; Richardson, T. J.; Milliron, D. J., Dynamically Modulating the Surface Plasmon Resonance of Doped Semiconductor Nanocrystals. *Nano Lett.* **2011**, *11*, 4415-4420.
8. Garcia, G.; Buonsanti, R.; Llordes, A.; Runnerstrom, E. L.; Bergerud, A.; Milliron, D. J., Near-Infrared Spectrally Selective Plasmonic Electrochromic Thin Films. *Adv. Opt. Mater.* **2013**, *1*, 215-220.
9. Wang, Y.; Runnerstrom, E. L.; Milliron, D. J., Switchable Materials for Smart Windows. *Ann. Rev. Chem. Biomol. Eng.* **2016**, *7*, 283-304.
10. Haes, A. J.; Hall, W. P.; Chang, L.; Klein, W. L.; Van Duyne, R. P., A Localized Surface Plasmon Resonance Biosensor: First Steps toward an Assay for Alzheimer's Disease. *Nano Lett.* **2004**, *4*, 1029-1034.
11. Runnerstrom, E. L.; Bergerud, A.; Agrawal, A.; Johns, R. W.; Dahlman, C. J.; Singh, A.; Selbach, S. M.; Milliron, D. J., Defect Engineering in Plasmonic Metal Oxide Nanocrystals. *Nano Lett.* **2016**, *16*, 3390-3398.
12. Tandon, B.; Ghosh, S.; Milliron, D. J., Dopant Selection Strategy for High-Quality Factor Localized Surface Plasmon Resonance from Doped Metal Oxide Nanocrystals. *Chem. Mater.* **2019**, *31*, 7752-7760.
13. Staller, C. M.; Robinson, Z. L.; Agrawal, A.; Gibbs, S. L.; Greenberg, B. L.; Lounis, S. D.; Kortshagen, U. R.; Milliron, D. J., Tuning Nanocrystal Surface Depletion by Controlling Dopant Distribution as a Route Toward Enhanced Film Conductivity. *Nano Lett.* **2018**, *18*, 2870-2878.

14. Staller, C. M.; Gibbs, S. L.; Saez Cabezas, C. A.; Milliron, D. J., Quantitative Analysis of Extinction Coefficients of Tin-Doped Indium Oxide Nanocrystal Ensembles. *Nano Lett.* **2019**, *19*, 8149-8154.
15. Tandon, B.; Agrawal, A.; Heo, S.; Milliron, D. J., Competition between Depletion Effects and Coupling in the Plasmon Modulation of Doped Metal Oxide Nanocrystals. *Nano Lett.* **2019**, *19*, 2012-2019.
16. Gibbs, S. L.; Staller, C. M.; Milliron, D. J., Surface Depletion Layers in Plasmonic Metal Oxide Nanocrystals. *Acc. Chem. Res.* **2019**, *52*, 2516-2524.
17. Gibbs, S. L.; Staller, C. M.; Agrawal, A.; Johns, R. W.; Saez Cabezas, C. A.; Milliron, D. J., Intrinsic Optical and Electronic Properties from Quantitative Analysis of Plasmonic Semiconductor Nanocrystal Ensemble Optical Extinction. *J. Phys. Chem. C* **2020**, *124*, 24351-24360.
18. Zandi, O.; Agrawal, A.; Shearer, A. B.; Reimnitz, L. C.; Dahlman, C. J.; Staller, C. M.; Milliron, D. J., Impacts of Surface Depletion on the Plasmonic Properties of Doped Semiconductor Nanocrystals. *Nat. Mater.* **2018**, *17*, 710-717.
19. Fang, H.; Hegde, M.; Yin, P.; Radovanovic, P. V., Tuning Plasmon Resonance of In<sub>2</sub>O<sub>3</sub> Nanocrystals throughout the Mid-Infrared Region by Competition between Electron Activation and Trapping. *Chem. Mater.* **2017**, *29*, 4970-4979.
20. Jansons, A. W.; Hutchison, J. E., Continuous Growth of Metal Oxide Nanocrystals: Enhanced Control of Nanocrystal Size and Radial Dopant Distribution. *ACS Nano* **2016**, *10*, 6942-6951.
21. Jansons, A. W.; Plummer, L. K.; Hutchison, J. E., Living Nanocrystals. *Chem. Mater.* **2017**, *29*, 5415-5425.
22. Shannon, R. D.; Prewitt, C. T., Effective Ionic Radii in Oxides and Fluorides. *Acta Crystallogr. Sec. B* **1969**, *25*, 925-946.
23. Tandon, B.; Yadav, A.; Khurana, D.; Reddy, P.; Santra, P. K.; Nag, A., Size-Induced Enhancement of Carrier Density, LSPR Quality Factor, and Carrier Mobility in Cr-Sn Doped In<sub>2</sub>O<sub>3</sub> Nanocrystals. *Chem. Mater.* **2017**, *29*, 9360-9368.
24. González, G. B.; Mason, T. O.; Quintana, J. P.; Warschkow, O.; Ellis, D. E.; Hwang, J.-H.; Hodges, J. P.; Jorgensen, J. D., Defect Structure Studies of Bulk and Nano-indium-tin oxide. *J. Appl. Phys.* **2004**, *96*, 3912-3920.
25. Lounis, S. D.; Runnerstrom, E. L.; Llordés, A.; Milliron, D. J., Defect Chemistry and Plasmon Physics of Colloidal Metal Oxide Nanocrystals. *J. Phys. Chem. Lett.* **2014**, *5*, 1564-1574.
26. Lounis, S. D.; Runnerstrom, E. L.; Bergerud, A.; Nordlund, D.; Milliron, D. J., Influence of Dopant Distribution on the Plasmonic Properties of Indium Tin Oxide Nanocrystals. *J. Am. Chem. Soc.* **2014**, *136*, 7110-7116.
27. Gibbs, S. L.; Dean, C.; Saad, J.; Tandon, B.; Staller, C. M.; Agrawal, A.; Milliron, D. J., Dual-Mode Infrared Absorption by Segregating Dopants within Plasmonic Semiconductor Nanocrystals. *Nano Lett.* **2020**, *20*, 7498-7505.
28. Thimsen, E.; Johnson, M.; Zhang, X.; Wagner, A. J.; Mkhoyan, K. A.; Kortshagen, U. R.; Aydil, E. S., High Electron Mobility in Thin Films Formed via Supersonic Impact Deposition of Nanocrystals Synthesized in Nonthermal Plasmas. *Nat. Commun.* **2014**, *5*, 5822.
29. Crockett, B. M.; Jansons, A. W.; Koskela, K. M.; Johnson, D. W.; Hutchison, J. E., Radial Dopant Placement for Tuning Plasmonic Properties in Metal Oxide Nanocrystals. *ACS Nano* **2017**, *11*, 7719-7728.
30. Hamberg, I.; Granqvist, C. G., Optical Properties of Transparent and Heat-Reflecting Indium Tin Oxide Films: The Role of Ionized Impurity Scattering. *Appl. Phys. Lett.* **1984**, *44*, 721-723.

## **Supporting Information**

### **Text S1: Nanocrystal Synthesis**

**Chemicals:** For the synthesis and characterization of different doped  $\text{In}_2\text{O}_3$  nanocrystals (NCs), all chemicals were acquired commercially and employed without further purification prior to their use. Indium(III) acetate (STREM,  $\geq 99.99\%$ ), titanium (IV) isopropoxide (Sigma-Aldrich 97%), cerium(III) acetylacetonate hydrate (Sigma-Aldrich 99.9%), zirconium(IV) acetylacetonate (Sigma-Aldrich, 97%), tin(IV) acetate (Sigma-Aldrich 99.99%), oleyl alcohol (Sigma-Aldrich, 85%) and oleic acid (Sigma-Aldrich, 90%) were used for the synthesis of different doped  $\text{In}_2\text{O}_3$  NCs. Oleylamine (Sigma-Aldrich, 70%), ethanol (Fischer Chemical, 90%), hexane (Fischer Chemical  $\geq 99.9\%$ ) and tetrachloroethylene (Sigma-Aldrich,  $\geq 99.9\%$ ) were utilized for washing the resulting nanocrystals and characterizing them through different techniques.

### **Synthesis Procedure:**

Doped  $\text{In}_2\text{O}_3$  NCs of different sizes but constant doping percentage were synthesized by minor modifications of the slow-injection synthetic procedure developed by the Hutchison group<sup>1</sup> and following similar literature reports.<sup>2-4</sup> In brief, on a standard Schlenk line apparatus, a 0.5 M mixture of In and dopant precursor in 10 mL oleic acid was degassed at 100 °C under vacuum conditions. This was followed by an undisturbed heating at 150 °C and constant stirring under  $\text{N}_2$  atmosphere for 2 hours. Using a syringe pump, different volumes of this mixture were subsequently injected into different flasks containing 13 mL oleyl alcohol kept at 290 °C (under  $\text{N}_2$  conditions) at the rate of 0.35 mL/min. Since in a slow-injection procedure, the size of the NC is dependent upon the amount of oleate precursor injected in the oleyl alcohol, injecting different volumes yielded NCs with a constant doping percentage but different sizes. Synthesized NCs were separated from the reaction mixture by repeated precipitation with anti-solvent ethanol, centrifugation at 9000 rpm for 5 min, and re-dispersing in hexane before finally being prepared as a colloidal dispersion of NCs in hexane. During each cycle of centrifugation, extra oleic acid and oleylamine were added as ligands to stabilize the NC dispersion. By changing the dopant precursor, different sizes of Sn-doped  $\text{In}_2\text{O}_3$  NCs, Zr-doped  $\text{In}_2\text{O}_3$  NCs, Ti-doped  $\text{In}_2\text{O}_3$  NCs and Ce-doped  $\text{In}_2\text{O}_3$  NCs with 1% overall doping percentage were prepared. The size and

polydispersity of the NCs was verified through scanning transmission electron microscopy (STEM) and the overall doping percentage was estimated through inductively coupled plasma optical emission spectroscopy (ICP-OES).

Additionally, we note here that all the dopants do not have the same incorporation efficiency in the  $\text{In}_2\text{O}_3$  lattice. Based on our previous reports, we have observed that Zr doping efficiency is 25% while Ce doping efficiency is 70% in the  $\text{In}_2\text{O}_3$  lattice. Therefore, their doping percentage in the precursor was raised accordingly to arrive at ~1% nominal doping concentration in the synthesized doped  $\text{In}_2\text{O}_3$  NCs.

### **Text S2: Nanocrystal Characterization**

**X-ray diffraction (XRD):** To determine the crystal structure and phase purity, a Rigaku Miniflex 600 instrument operating in a Bragg-Brentano geometry with  $\text{Cu K}\alpha$  ( $\lambda = 1.5406 \text{ \AA}$ ) as the X-ray source was employed to record powder XRD patterns of as-synthesized NCs deposited on a small piece of Si wafer.

**Transmission electron microscopy (TEM):** The average NC diameter, polydispersity and morphology of the doped  $\text{In}_2\text{O}_3$  NCs was examined through low-resolution scanning TEM (STEM) microscopy on a Hitachi S5500 operating at an accelerating voltage of 30 mV in the STEM mode. Sample preparation involved drop-casting followed by air-drying 20  $\mu\text{L}$  dilute solution of NCs in hexane (~15 mg/mL of NCs in 1 mL hexane) on a copper 300 mesh TEM grid. The average NC diameter and standard deviation in sizes of different NCs were determined by analyzing 200-300 particles from their respective STEM images using ImageJ software and fitting the statistics to a Gaussian size distribution.

**Inductively coupled plasma-optical emission spectroscopy (ICP-OES):** Doping percentages of different dopants in  $\text{In}_2\text{O}_3$  and volume fraction of NCs in solution was experimentally determined by utilizing ICP-OES technique on a Varian 720-ES ICP Optical Emission Spectrometer. Samples for the ICP-OES were prepared by digesting a known volume of the stock solution of NC in aqua-regia solution (a mixture of 35% concentrated  $\text{HCl}$  and 70%  $\text{HNO}_3$  in 3:1 ratio respectively) for 48 hours. This was followed by diluting the acid solution with milli-Q water such that the total acid concentration becomes approximately 2% v/v. Standard solutions of variable concentration for different elements were prepared by diluting the commercial ICP-OES standard with 2%  $\text{HNO}_3$

solution in milli-Q water. The doping percentage was calculated as a mole fraction of the dopant with respect to the total metal concentration (In + dopant) obtained in the ICP. The volume fraction of doped In<sub>2</sub>O<sub>3</sub> NCs was calculated from the concentration of In and dopant in the analyte using an assumed stoichiometry of (In+dopant)<sub>2</sub>O<sub>3</sub> and density of 7140 mg/mL.

**X-ray photoelectron spectroscopy (XPS):** To develop an understanding about the radial distribution of dopants within the NCs, XPS spectra of different NCs were recorded on a Kratos X-ray Photoelectron Spectrometer – Axis Ultra DLD using a monochromatic Al K $\alpha$  radiation ( $\lambda = 1486.6$  eV) and a charge neutralizer. The XPS spectra obtained for different elements were calibrated by fixing the adventitious C1s peak to 284.8 eV binding energy and analyzed through CasaXPS software. Doping percentages for different dopants were calculated by taking a ratio of the integrated area under the dopant peak with the combined area under the In 3d and the dopant XPS peaks while taking into consideration the sensitivity factors of the different elements involved.

**Optical Spectroscopy:** For optical spectroscopy measurements, stock solution of all NCs were prepared in a solution of 1.8 mM oleic acid in tetrachloroethylene (TCE). These stock solutions were then diluted right before the optical measurement and their dilution factors calculated through mass fractions of stock to total solution for each sample. The diluted stock solution of NCs in TCE was injected through a syringe in a liquid cell having a path length of 0.5 mm. Their infrared extinction spectra were then collected on a Bruker Vertex 70 FTIR spectrophotometer. All spectra were measured in the transmission mode and reported as extinction. NC spectra were backgrounded to a clean solution of 1.8 mM oleic acid in TCE before starting each dilution series. To confirm the lack of NC deposition, the liquid cell was washed repeatedly through 1.8 mM oleic acid in TCE after each dilution series measurement and subsequent collection of an after spectrum. All reported series here do not show any deposition on the KBr windows of liquid cell.

### **Text S3: Heterogeneous Ensemble Drude Approximation (HEDA) Model**

A detailed discussion of this code and a copy of the MATLAB script that runs the code can be found in reference 17 in the main text. In short, the HEDA model extracts the optoelectronic properties of the average NC in an heterogeneous ensemble of NCs. To do this, one must prepare a dilute dispersion of NCs, such that the NCs are not interacting with one another, and collect the optical response near the LSPR peak frequency. The HEDA model can fit the plasmonic response

of isotropic, spherical plasmonic nanoparticles by fitting for four parameters: the average charge carrier concentration  $\mu_{n_e}$ , the standard deviation in a normal distribution of charge carrier concentrations  $\sigma_{n_e}$ , the mean free path of a charge carrier  $l_{MFP}$ , and the electron accessible volume fraction  $f_e$ . This model requires the input of the volume fraction of NCs in the dispersion  $f_v$ , the average diameter  $\mu_r$ , and the standard deviation in diameter  $\sigma_r$ , as well as some other known optical constants. A successful fitting procedure enables the determination of the properties of an average NC in an ensemble, unclouded by the effects of heterogeneity.

In our fitting procedure we needed to place upper bounds on the fit parameter  $l_{MFP}$  and lower bounds on the fit parameter  $\sigma_{n_e}$ . The upper bound on  $l_{MFP}$  is required because as the NC radius decreases, becoming much smaller than the mean free path, surface scattering becomes so dominant that the contribution from bulk damping becomes negligible and therefore fitting for  $l_{MFP}$  becomes difficult as the value tends to go to infinity to eliminate the bulk damping contribution altogether. Therefore we placed a reasonable fit constraint of 25 nm for dopants other than Sn. For Sn there is extensive literature for the bulk film such that we knew 17 nm was a reasonable upper limit for the  $l_{MFP}$ . Knowing that changing dopants has the ability to reduce damping (increase  $l_{MFP}$ ) we felt 25 nm ( $\sim 1.5x$ ) was a safe upper bound for other dopants.

The lower bound that we placed on  $\sigma_{n_e}$  is based on Poissonian statistics expected for dopant incorporation into NCs. The minimum standard deviation, as governed by a Poissonian distribution, in the number of dopants in a single NC  $N_d$  within an ensemble follows the relationship:  $\sigma_{N_d} \approx \sqrt{\mu_{N_d}}$ . After using ICP-AES to quantify the concentration of dopants in the average NC, we then set the lower bound for  $\sigma_{n_e}$  to be  $\sqrt{\mu_{N_d}}$ .

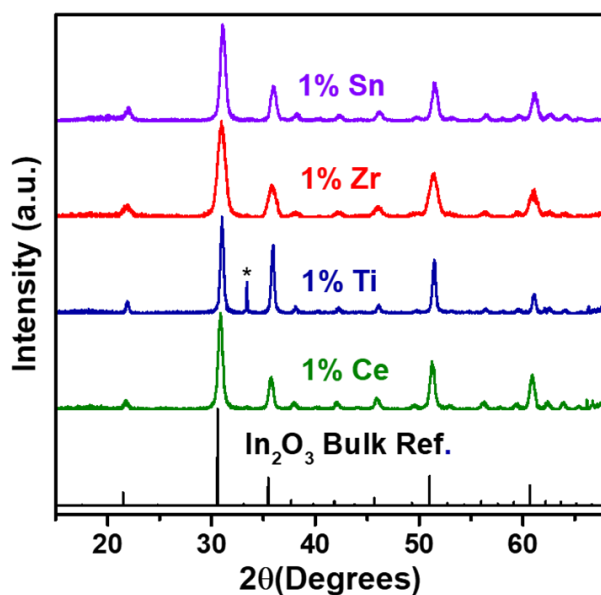


**Figure S1:** X-ray diffraction patterns of different 1% doped  $\text{In}_2\text{O}_3$  NCs showing phase pure NCs exhibiting the same cubic bixbyite structure as the bulk reference (JCPDS 88-2160). The diffraction peaks marked with \* belong to the Si substrate.

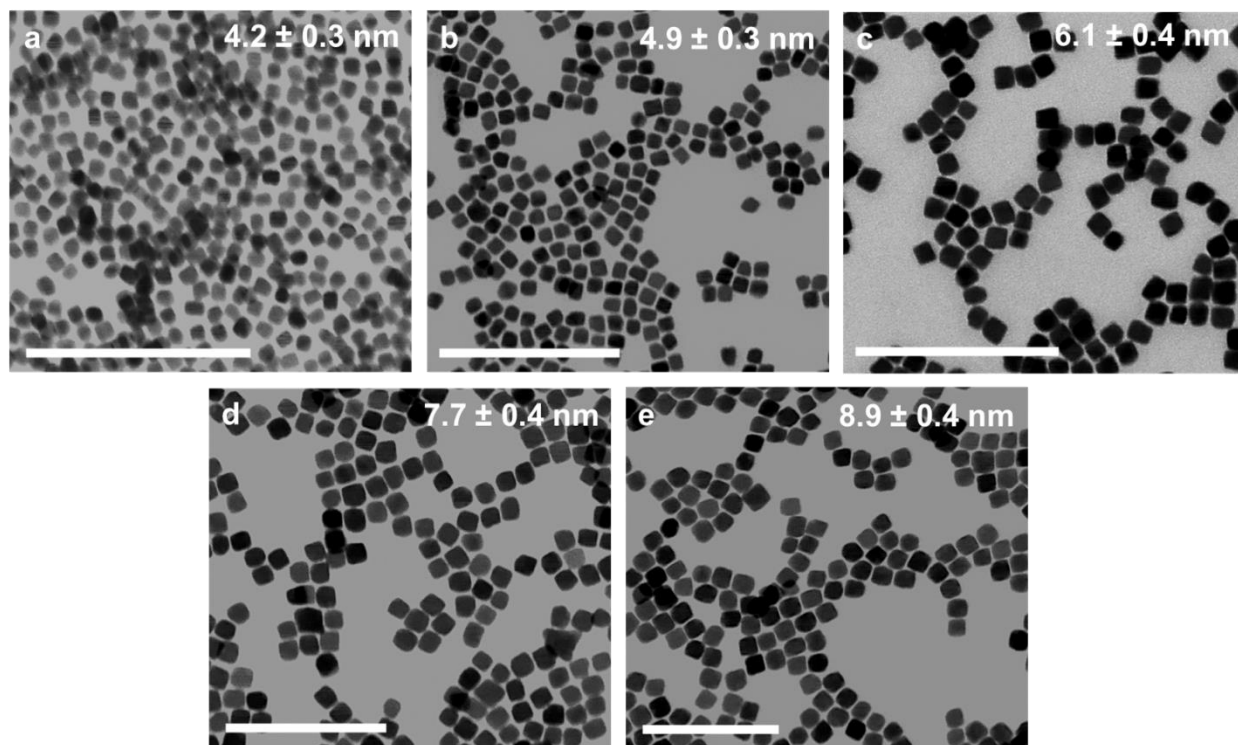


**Figure S2:** STEM images of 1% Sn-doped  $\text{In}_2\text{O}_3$  NCs with different radius. All scale bars are 100 nm.

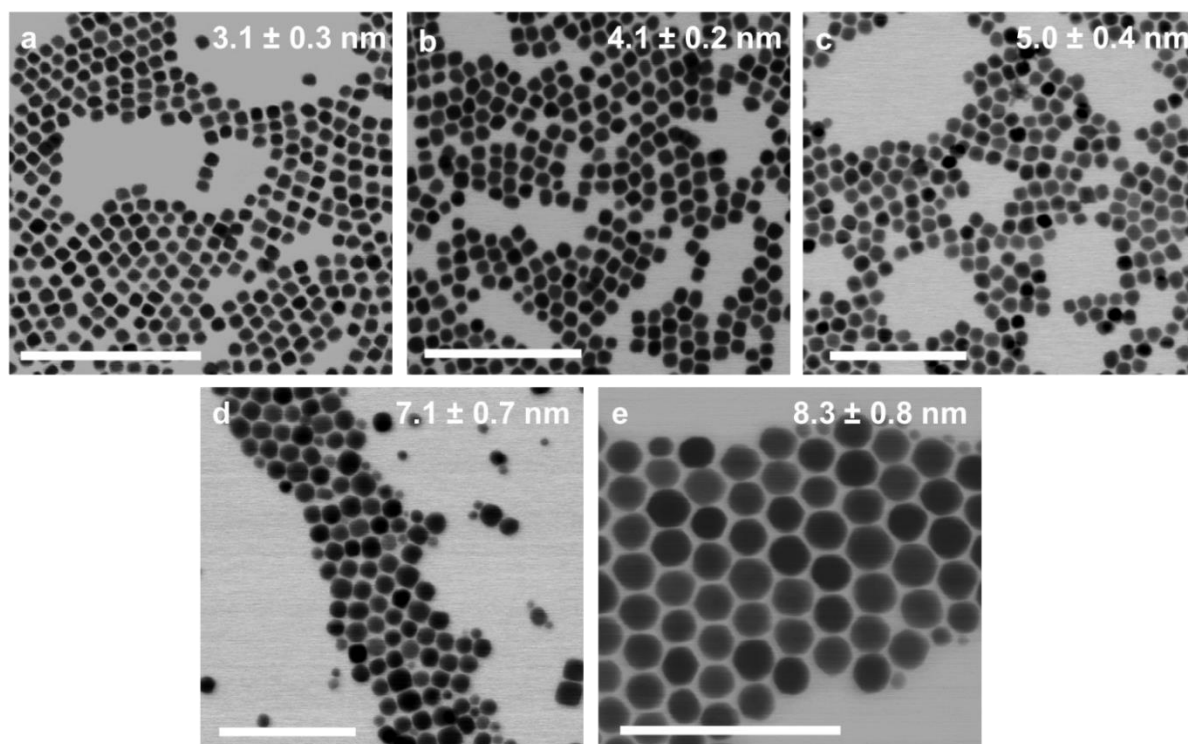


**Figure S3:** STEM images of 1% Zr-doped  $\text{In}_2\text{O}_3$  NCs with different radius. All scale bars are 100 nm.

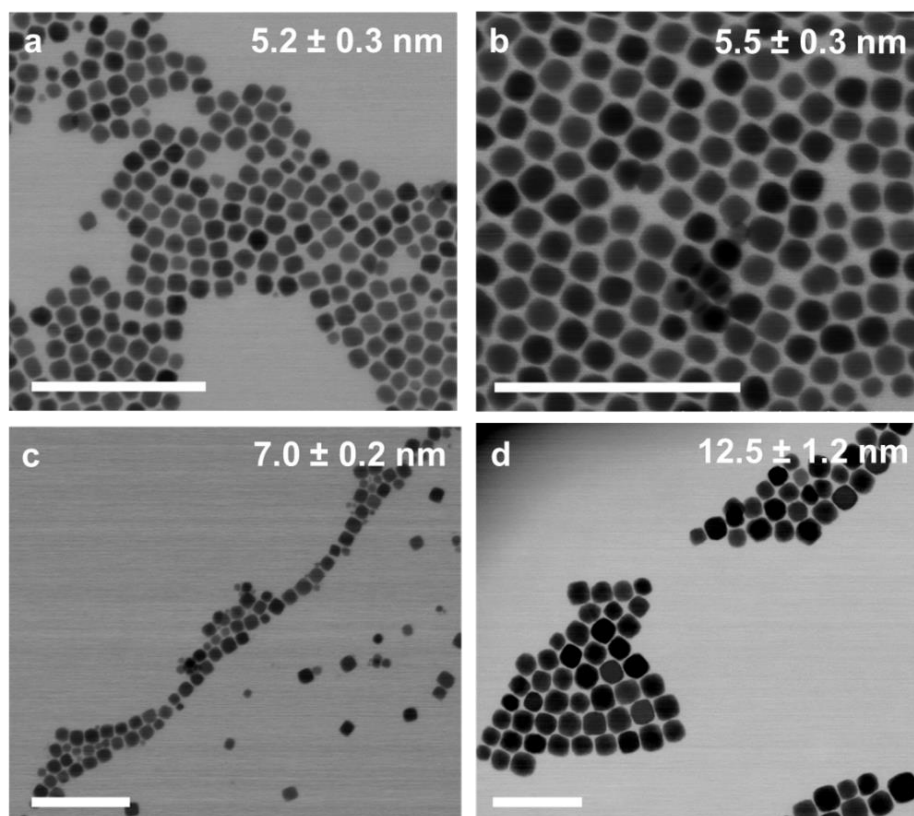


**Figure S4:** STEM images of 1% Ti-doped  $\text{In}_2\text{O}_3$  NCs with different radius. All scale bars are 100 nm.

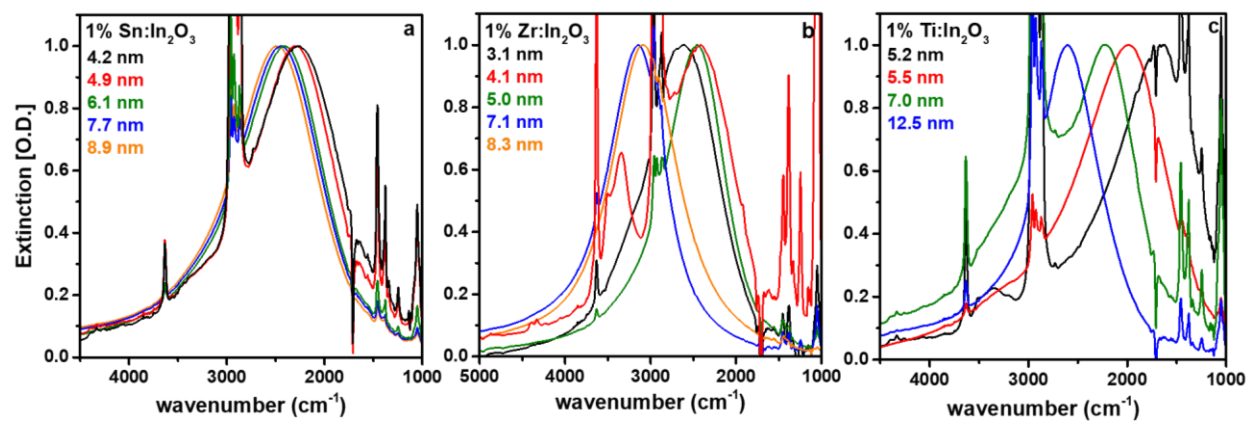


**Figure S5:** Normalized extinction spectra, for (a) 1% Sn:In<sub>2</sub>O<sub>3</sub> NCs (b) 1% Zr:In<sub>2</sub>O<sub>3</sub> NCs and (c) 1% Ti:In<sub>2</sub>O<sub>3</sub> NCs of increasing radius.

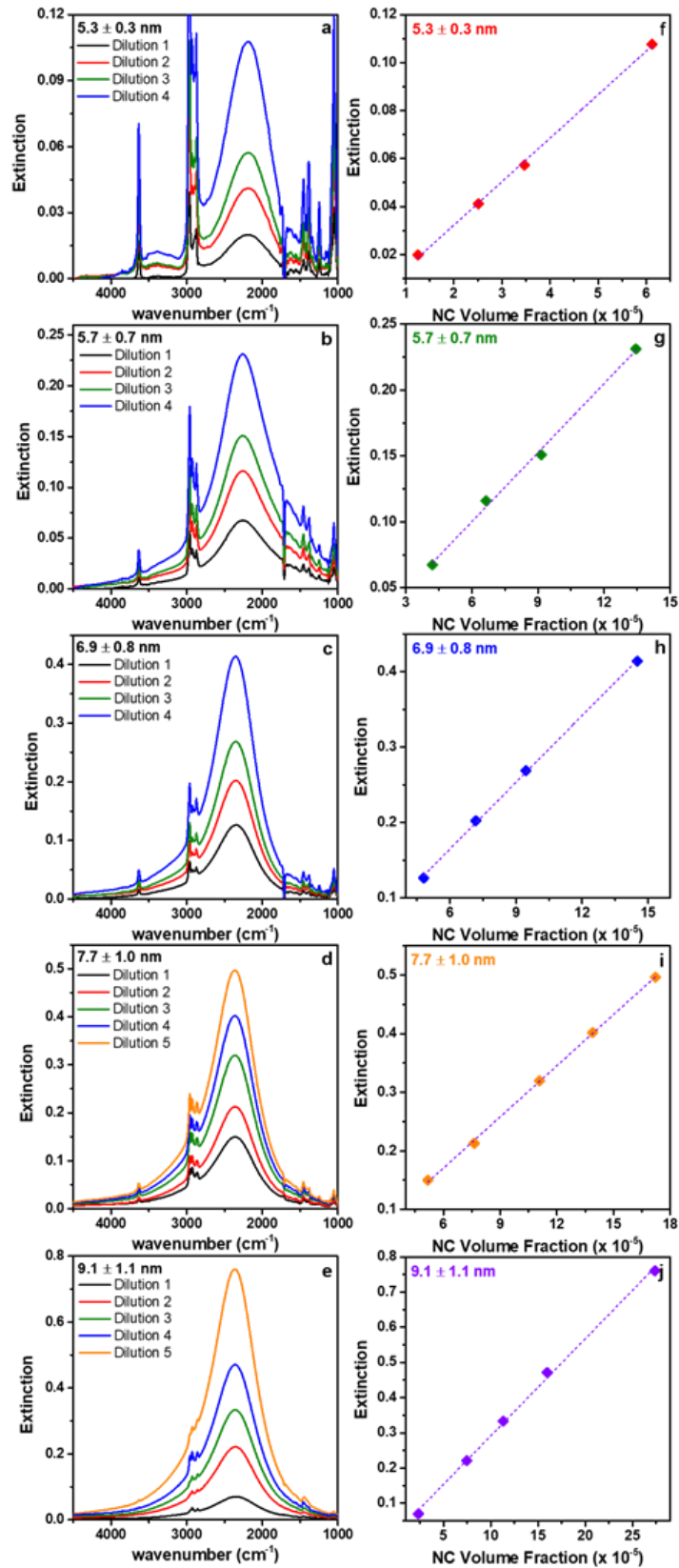


**Figure S6:** (a-e) Extinction spectra of different dilutions (f-j) Beer-Lambert's curves for 1% Ce:In<sub>2</sub>O<sub>3</sub> NCs with increasing radius.

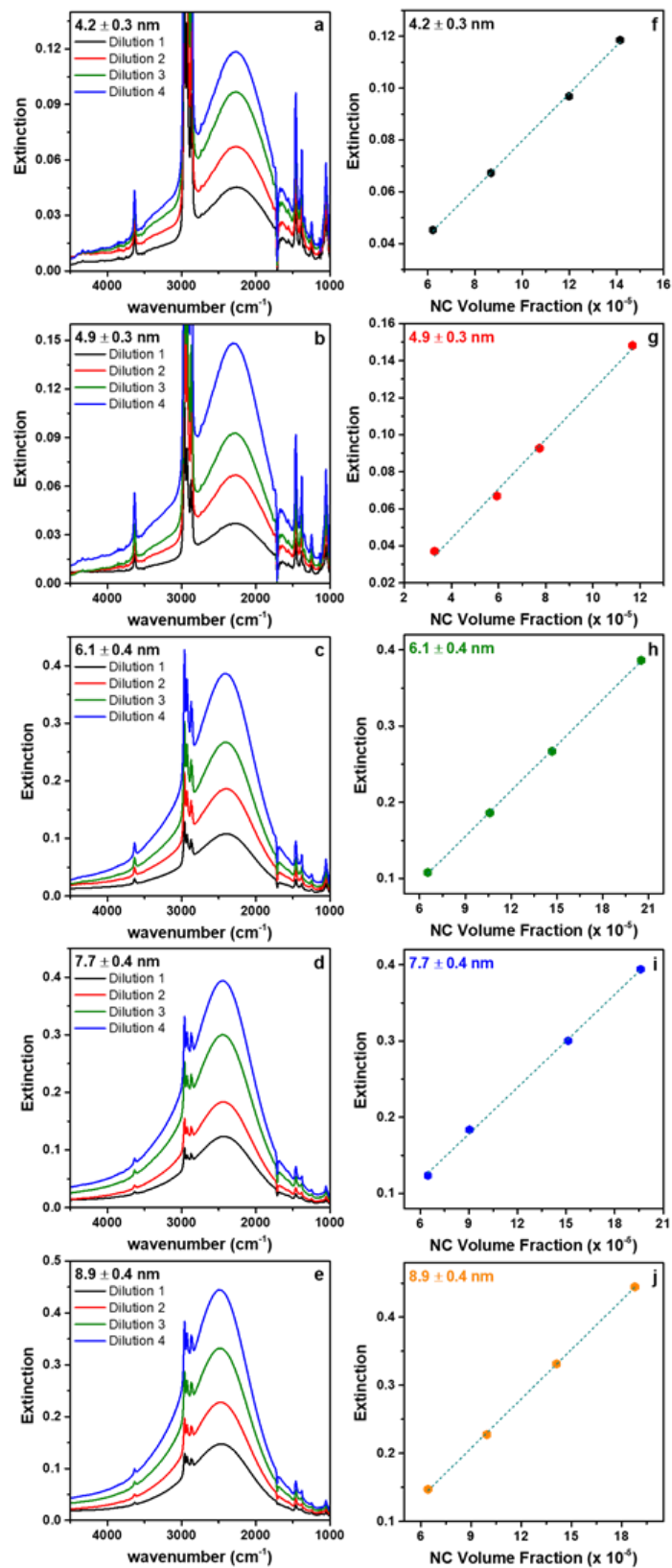


**Figure S7:** (a-e) Extinction spectra of different dilutions (f-j) Beer-Lambert's curves for 1% Sn:In<sub>2</sub>O<sub>3</sub> NCs with increasing radius.

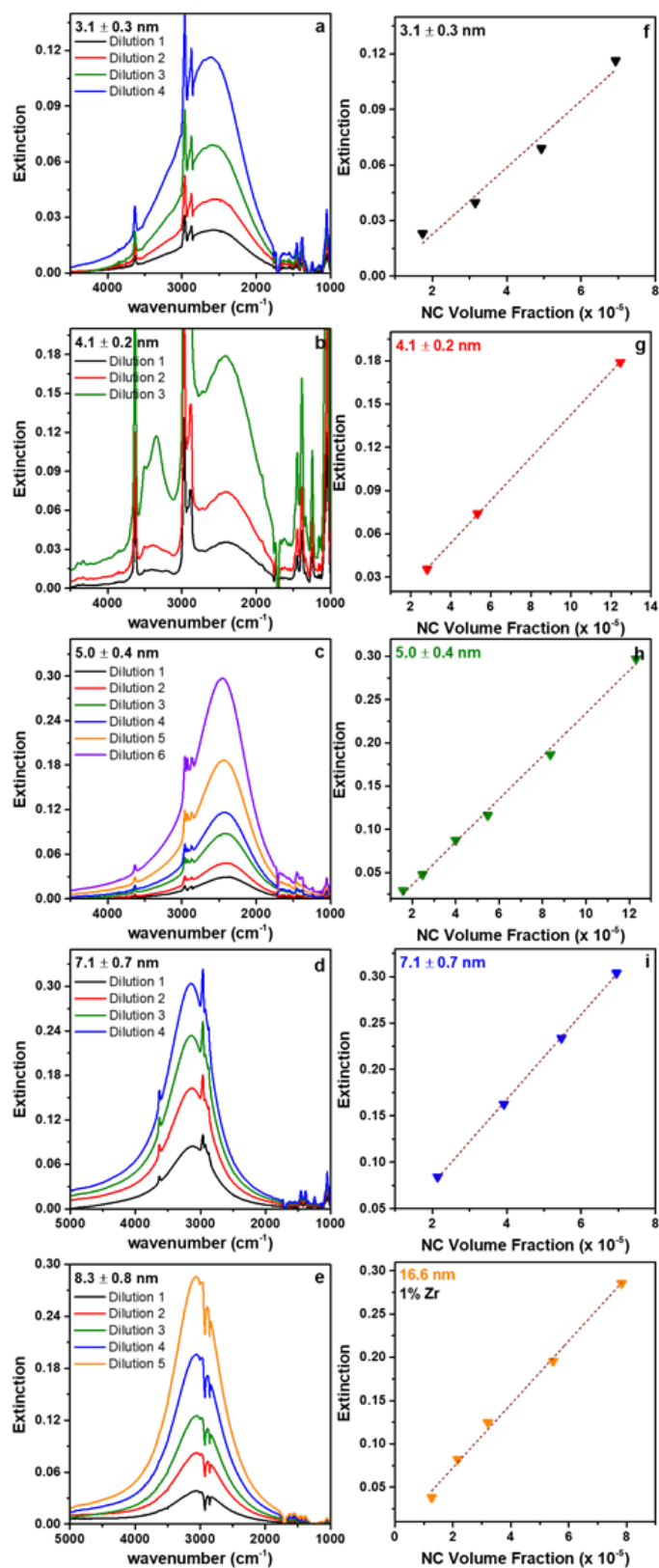


**Figure S8:** (a-e) Extinction spectra of different dilutions (f-j) Beer-Lambert's curves for 1% Zr:In<sub>2</sub>O<sub>3</sub> NCs with increasing radius.

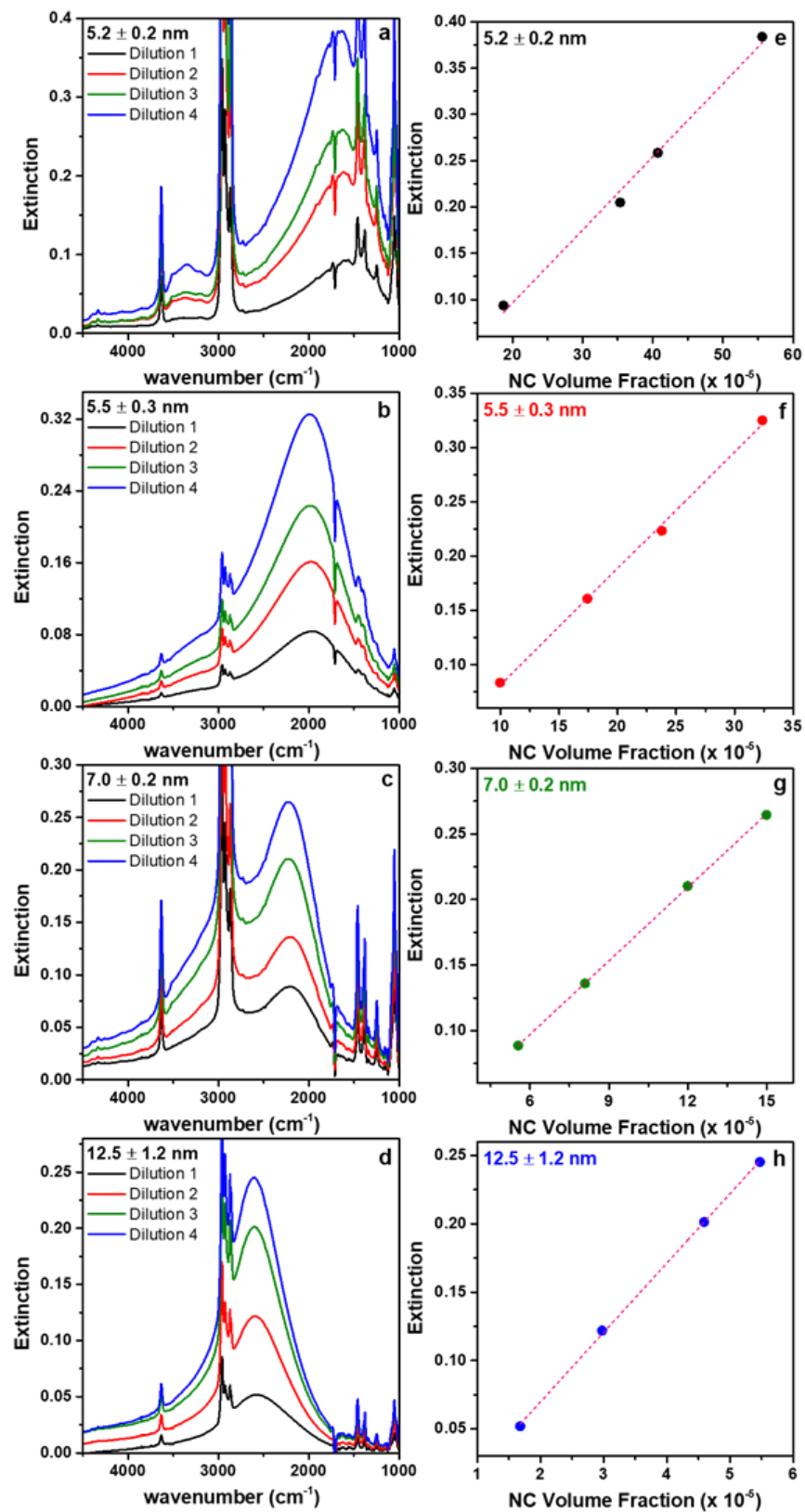


**Figure S9:** (a-e) Extinction spectra of different dilutions (f-j) Beer-Lambert's curves for 1% Ti:In<sub>2</sub>O<sub>3</sub> NCs with increasing radius.

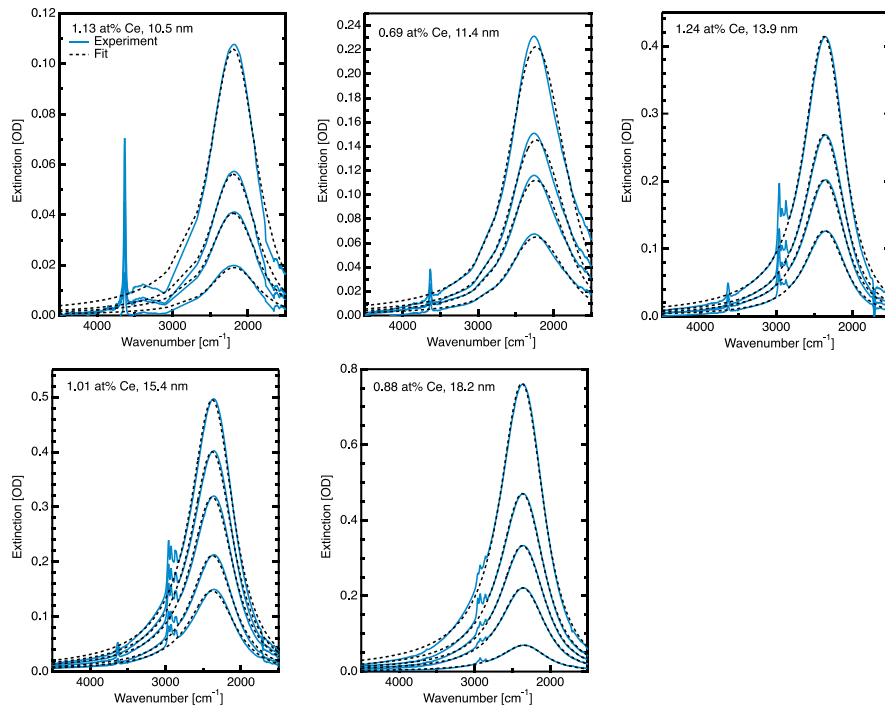


**Figure S10:** Experimental extinction spectra (blue solid lines) and HEDA fits (black dashed lines) for all samples and dilutions of the Ce-doped  $\text{In}_2\text{O}_3$  series.

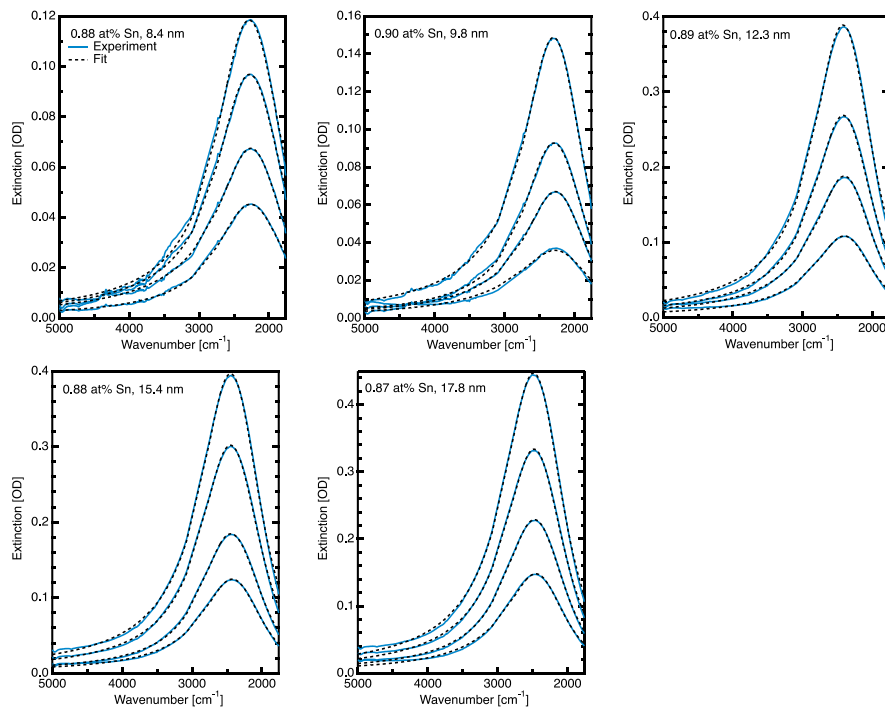


**Figure S11:** Experimental extinction spectra (blue solid lines) and HEDA fits (black dashed lines) for all samples and dilutions of the Sn-doped  $\text{In}_2\text{O}_3$  series.

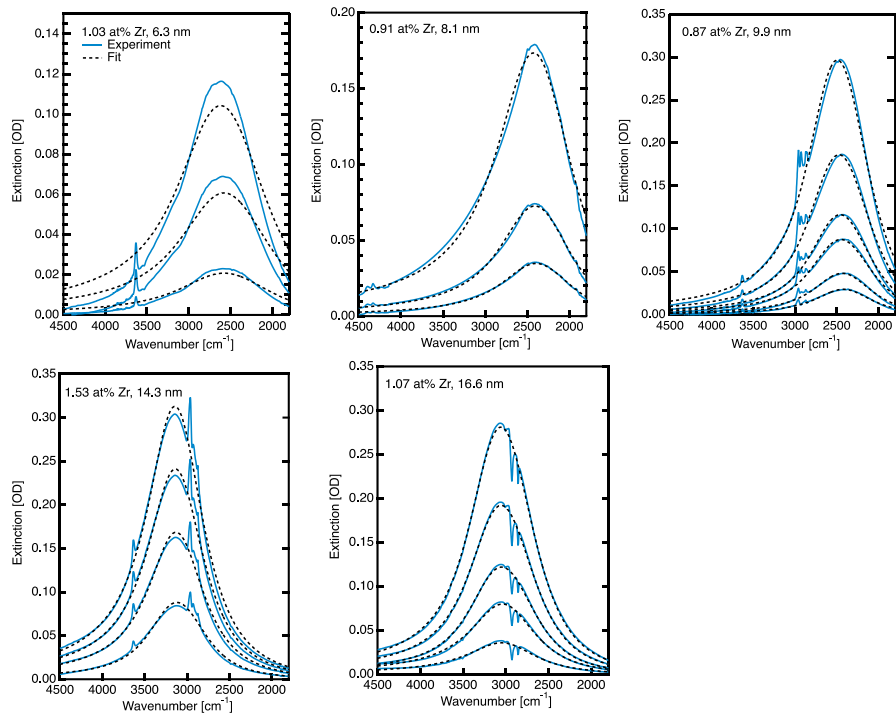


**Figure S12:** Experimental extinction spectra (blue solid lines) and HEDA fits (black dashed lines) for all samples and dilutions of the Zr-doped  $\text{In}_2\text{O}_3$  series.

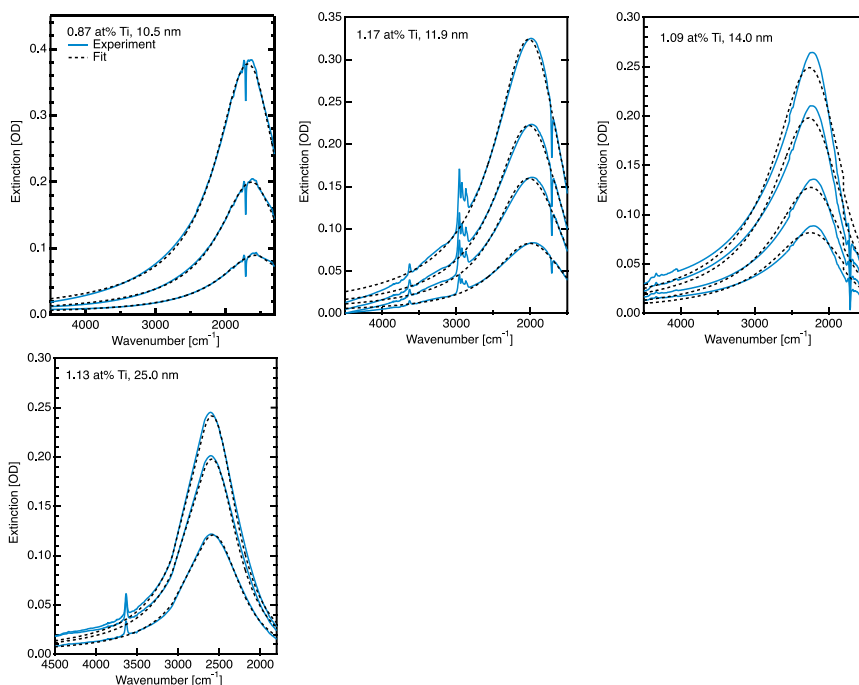


**Figure S13:** Experimental extinction spectra (blue solid lines) and HEDA fits (black dashed lines) for all samples and dilutions of the Ti-doped  $\text{In}_2\text{O}_3$  series.

## References:

1. Jansons, A. W.; Hutchison, J. E., Continuous Growth of Metal Oxide Nanocrystals: Enhanced Control of Nanocrystal Size and Radial Dopant Distribution. *ACS Nano* **2016**, *10*, 6942-6951.
2. Tandon, B.; Ghosh, S.; Milliron, D. J., Dopant Selection Strategy for High-Quality Factor Localized Surface Plasmon Resonance from Doped Metal Oxide Nanocrystals. *Chem. Mater.* **2019**, *31*, 7752-7760.
3. Runnerstrom, E. L.; Bergerud, A.; Agrawal, A.; Johns, R. W.; Dahlman, C. J.; Singh, A.; Selbach, S. M.; Milliron, D. J., Defect Engineering in Plasmonic Metal Oxide Nanocrystals. *Nano Lett.* **2016**, *16*, 3390-3398.
4. Fang, H.; Hegde, M.; Yin, P.; Radovanovic, P. V., Tuning Plasmon Resonance of  $\text{In}_2\text{O}_3$  Nanocrystals throughout the Mid-Infrared Region by Competition between Electron Activation and Trapping. *Chem. Mater.* **2017**, *29*, 4970-4979.

### For Table of Contents Only

